RSC Advances

PAPER

View Article Online
View Journal | View Issue

Cite this: *RSC Adv.*, 2026, **16**, 10785

Synthesis and zero-dimensional structure of a new lead-free organic–inorganic $[(C_2H_5)_4N]_3Bi_2I_9$ compound: a promising material for optoelectronic devices

Hanen Elgahami, [a] Khawla Ben Brahim, [a] Sondes Hajlaoui,[a] Mona A. Alamri,[b] Gwenaël Corbel [c] and Abderrazek Oueslati *[a]

A new lead-free organic–inorganic hybrid compound based on Bi(III), namely tris(tetraethylammonium) nona-idodibismuthate(III), $[(C_2H_5)_4N]_3Bi_2I_9$, has been successfully synthesized using a slow evaporation technique. The compound was characterized by single-crystal X-ray diffraction, Hirshfeld surface analysis, thermal analyses (DSC and TGA-DTA) and impedance spectroscopy. At room temperature, it crystallizes in the triclinic system with *P*1 space group. The crystal structure consists of discrete anionic dimers $[Bi_2I_9]^{3-}$. These dimers are formed by two BiI_6 octahedra sharing a triangular face. Charge balance is ensured by three $[(C_2H_5)_4N]^+$ cations. The organic and inorganic components are connected through C–H···I hydrogen bonds. These interactions lead to the formation of a stable three-dimensional supramolecular network. Hirshfeld surface analysis shows that H···I/I···H and H···H interactions dominate the intermolecular contacts. Weak I···I interactions also contribute to the structural cohesion. Thermal analyses (DSC and TGA/DTA) reveal a reversible phase transition in the temperature range of 331–340 K. No weight loss is observed during this transition. This behavior may affect the electrical properties of the compound and enhance its potential for temperature-dependent electronic applications. Nyquist plots display a single semicircular arc, which is characteristic of non-Debye relaxation. The AC conductivity follows Jonscher's universal power law. These results indicate thermally activated charge transport governed by the correlated barrier hopping (CBH) model.

Received 3rd December 2025
Accepted 16th February 2026

DOI: 10.1039/d5ra09365a

rsc.li/rsc-advances

1. Introduction

Over the past several years, alkylammonium and halobismuthate(III) compounds have attracted considerable attention due to their potential applications in photovoltaic technology and optoelectronics. This interest arises from their easy solution processing and low production costs.[1–3] Numerous structural studies have shown that Bi(III) halide derivatives incorporating different organic amines exhibit a wide diversity of anionic frameworks.[4–9] Within this broad class of organic–inorganic hybrid materials, various structural dimensionalities have been reported, including zero-dimensional (0D), one-dimensional (1D), and two-dimensional (2D) architectures. In contrast, three-dimensional (3D) networks remain relatively rare. Among these materials, compounds with the general formula $R_3M_2X_9$ and $R_5M_2X_{11}$ (where R is an organic amine, M = Bi(III) and X = Cl, Br, or I) are of particular interest. These compounds often exhibit ferroelectric and ferroelastic properties.[10–13] Iodine-based members of the $R_3M_2X_9$ family generally adopt a zero-dimensional structure composed of anionic dimers $[Bi_2I_9]^{3-}$. These dimers are formed by two BiI_6 octahedra sharing a triangular face, as observed in $(CH_3NH_3)_3Bi_2I_9$. Compounds of the $R_3M_2I_9$ type, which contain discrete $[M_2I_9]^{3-}$ anions, are particularly attractive. They combine promising electro-optic properties with enhanced chemical stability, making them suitable candidates for lead-free photovoltaic materials.[14,15] Iodobismuthates(III), with the general formula $R_3Bi_2I_9$, represent an important subclass from an application perspective. They offer facile synthesis, cost efficiency, and favorable electrical and optical properties.[16,17] Previous investigations have demonstrated that the nature and size of the organic cation strongly influence crystal packing and intermolecular interactions. These variations also affect key physical properties, including thermal stability and electrical transport behavior.[18–20] Comparative studies between methylammonium-based iodobismuthates and analogues containing bulkier organic cations have revealed significant

[a]*Laboratory for Spectroscopic Characterization and Optics of Materials, Faculty of Sciences, University of Sfax, B. P. 1171, 3000, Sfax, Tunisia. E-mail: oueslatiabderrazek@yahoo.fr*

[b]*Department of Chemistry, College of Science, Qassim University, Buraidah 51452, Saudi Arabia*

[c]*Institut des Molécules et Matériaux du Mans (IMMM), UMR-6283 CNRS, Le Mans Université, Avenue Olivier Messiaen, 72085, Le Mans Cedex 9, France*

differences in lattice dynamics and organic–inorganic coupling. These differences directly impact dielectric response and charge transport mechanisms.[21,22] In general, compounds incorporating larger organic cations exhibit improved thermal stability and modified dielectric or conduction behavior. This behavior is attributed to changes in hydrogen-bonding networks, lattice flexibility, and reduced structural disorder.[23–25] A distinctive feature of these materials is the presence of a stereochemically active lone electron pair ($5s^2$ for Sb and $6s^2$ for Bi). Although this lone pair exerts only a moderate influence on structural geometry, it plays a crucial role in determining physical properties. In particular, it strongly affects polarization-related effects and charge transport behavior.[26] Motivated by the intriguing properties of $(CH_3NH_3)_3Bi_2I_9$ and related analogues, we investigated the effect of replacing methylammonium cation with the larger tetraethylammonium cation. The aim was to evaluate the resulting changes in structure and physical properties. In this work, we report the synthesis, single-crystal X-ray structure determination, Hirshfeld surface analysis, thermal behavior and electrical properties of a new member of the $R_3M_2I_9$ family: $[(C_2H_5)_4N]_3Bi_2I_9$.

2. Experimental details

All starting materials employed for the synthesis of $[(C_2H_5)_4N]_3Bi_2I_9$ were purchased from commercial suppliers and used without further purification. Tetraethylammonium iodide $[(C_2H_5)_4N]I$ (98%) and bismuth(III) iodide BiI_3 (99%) were obtained from Sigma-Aldrich, while hydroiodic acid HI (57%) was purchased from Merck. Single crystals of $[(C_2H_5)_4N]_3Bi_2I_9$ were grown by a slow evaporation method at room temperature. Stoichiometric amounts of $[(C_2H_5)_4N]I$ and BiI_3 were dissolved in 10 mL of HI (57%). The resulting solution had an approximate concentration of 7.5 M. A few drops of methanol or acetone were added to aid facilitate dissolution. The resulting solution was placed in glass Petri dishes and allowed to evaporate slowly at approximately 23 °C. After 3–4 days, red crystals suitable for structural characterization were obtained.

The chemical reaction can be schematically represented as follows:

$$3\left[(C_2H_5)_4N\right]I + 2BiI_3 \xrightarrow{HI} \left[(C_2H_5)_4N\right]_3Bi_2I_9 \quad (1)$$

A suitable single crystal of $[(C_2H_5)_4N]_3Bi_2I_9$ was selected under an optical microscope and mounted on MicroMount needles (MiTiGen) for single-crystal X-ray diffraction analysis. X-ray intensity data were collected at 296 K using a Bruker APEX II Quazar diffractometer. The instrument was equipped with four-circle Kappa goniometer and a CCD detector. Data collection was performed with a a microfocus Mo-Kα radiation source ($\lambda = 0.71073$ Å). An absorption correction was applied using the multi-scan method implemented in SADABS.[27] The structure was solved by direct methods and refined through successive difference Fourier maps. Full-matrix least-squares refinement was carried out on all $|F|^2$ data using SHELX program[28] suite within the WinGX interface.[29] Structural graphics were generated using the Diamond 3.2 software.[30] The crystal structure of the title compound was resolved in the triclinic system, with non-centrosymmetric space group $P1$ (no. 1). All non-hydrogen atoms were refined anisotropically. While hydrogen atoms attached to the amine groups were geometrically constrained using the HFIX option. Crystallographic data and refinement details are summarized in Table 1. Selected bond lengths and angles are presented in Tables 2 and 3. Further crystallographic information for this compound is available from the Cambridge Crystallographic Data Centre (CCDC 2457063).

Hirshfeld surface (HS) analysis was performed using the CrystalExplorer 17.5 software package.[31] The analysis used the crystal structure input file in CIF format. Intermolecular interactions were visualized on the Hirshfeld surface mapped over the normalized contact distance (d_{norm}). A red–white–blue color was used to represent intermolecular contacts that are shorter, equal to, or longer than the corresponding van der Waals separations, respectively. For each point on the HS, two parameters were defined: d_i (the distance from the surface point to the nearest nucleus inside the surface) and d_e (the distance to the nearest nucleus outside the surface). The normalized contact distance (d_{norm}), was calculated using d_i, d_e, and the van der Waals radii of the atoms. It was calculated according to the following equation:

$$d_{norm} = \frac{d_{i-}\, r_i^{vdw}}{r_i^{vdw}} + \frac{d_{e-}\, r_e^{vdw}}{r_e^{vdw}} \quad (2)$$

where r_i^{vdw} is the van der Waals radius of the atom located inside the Hirshfeld surface, and revdw is the van der Waals radius of the atom located outside the surface. Two-dimensional (2D) fingerprint plots were generated from the d_{norm}-mapped

Table 1 Crystallographic data and structure refinement parameters for $[(C_2H_5)_4N]_3Bi_2I_9$

Empirical formula	$[(C_2H_5)_4N]_3Bi_2I_9$
Formula weight (g mol^{-1})	1950.81
Crystal system, space group	Triclinic, $P1$
Temperature (K)	296
a (Å)	11.1244(4)
b (Å)	11.1286(4)
c (Å)	12.4964(5)
α (°)	88.894(2)
β (°)	64.702(1)
γ (°)	61.479(1)
V (Å^3)	1195.24(8)
Z	1
Radiation type	Mo Kα
λ (Å)	0.71073
Measured reflections	14 631
Independent reflections	3682
Observed reflections ($I > 2\sigma(I)$)	3626
$F(000)$	868
Dcal (Mg m^{-3})	2.710
Index ranges	$h = -10 \rightarrow 10$; $k = -10 \rightarrow 10$; $l = -11 \rightarrow 11$
Number of parameters	353
R_1	0.017
wR_2	0.045
Goodness of fit (S)	0.82

Table 2 Selected bond distances (Å) and bond angles (°) for inorganic part $[Bi_2I_9]^{3-}$

Distance (Å)		Angle (°)
Bi1–I1	2.948(1)	I9–Bi1–I1 94.29(4)
Bi1–I8	2.976(1)	I9–Bi1–I8 93.46(3)
Bi1–I9	2.934(1)	I1–Bi1–I8 91.09(3)
Bi1–I2	3.280(1)	I9–Bi1–I6 89.28(3)
Bi1–I4	3.253(1)	I1–Bi1–I6 92.40(3)
Bi1–I6	3.200(1)	I8–Bi1–I6 175.38(4)
Bi2–I4	3.252(1)	I9–Bi1–I4 91.56(3)
Bi2–I2	3.288(1)	I1–Bi1–I4 173.16(4)
Bi2–I6	3.299(1)	I8–Bi1–I4 92.10(3)
Bi2–I3	2.934(1)	I6–Bi1–I4 84.12(3)
Bi2–I5	2.940(1)	I9–Bi1–I2 170.27(4)
Bi2–I7	2.947(1)	I1–Bi1–I2 91.81(3)
—	—	I8–Bi1–I2 93.99(3)
—	—	I6–Bi1–I2 82.89(3)
—	—	I4–Bi1–I2 81.94(3)
—	—	I3–Bi2–I5 94.68(4)
—	—	I3–Bi2–I7 94.53(4)
—	—	I5–Bi2–I7 93.35(4)
—	—	I3–Bi2–I2 169.89(4)
—	—	I7–Bi2–I2 92.46(4)
—	—	I4–Bi2–I2 81.84(3)
—	—	I3–Bi2–I6 172.18(4)
—	—	I5–Bi2–I6 90.35(4)
—	—	I7–Bi2–I6 91.15(4)
—	—	I4–Bi2–I6 82.58(3)
—	—	I2–Bi2–I6 81.26(3)

Table 3 Principal bond distances (Å) and bond angles (°) of organic part in $[(C_2H_5)_4N]^+$

Distance (Å)			
N1–C17	1.502	C13–C14	1.510
N1–C13	1.502	C26–C25	1.470
		C26–C25	
N1–C15	1.515	C21–C22	1.560
N1–C11	1.540	C28–C27	1.460
N2–C21	1.494	C23–C24	1.500
N2–C27	1.496	C38–C37	1.590
N2–C25	1.504	C37–N3	1.460
N2–C23	1.523	N3–C31	1.450
C34–C33	1.440	N3–C35	1.480
C12–C11	1.530	N3–C33	1.480
		N3–C33	
C15–C16	1.460	C35–C36	1.730
C17–C18	1.500	C32–C31	1.470
Angle (°)			
C17–N1–C15	110.4	C26–C25–N2	118.1
C13–N1–C15	107.8	N2–C21–C22	115.4
C17–N1–C11	108.6	C28–C27–N2	118.2
C13–N1–C11	111.7	C24–C23–N2	117.0
C15–N1–C11	107.5	N3–C37–C38	115.0
C21–N2–C27	107.7	C31–N3–C37	111.9
C21–N2–C25	109.7	C31–N3–C35	110.2
C27–N2–C25	109.3	C37–N3–C35	116.0
C21–N2–C23	111.2	C31–N3–C33	106.5
C27–N2–C23	108.9	C37–N3–C33	107.0
C25–N2–C23	109.9	C35–N3–C33	103.9
C12–C11–N1	115.0	N3–C35–C36	109.0
C16–C15–N1	116.1	N3–C31–C32	117.0
C18–C17–N1	116.3	C34–C33–N3	120.0
C17–N1–C13	110.7	N1–C13–C14	115.6

Hirshfeld surface. These plots provide a quantitative representation of the different intermolecular interactions present within in the crystal structure. These plots illustrate the frequency distribution of d_i and d_e distance pairs over the Hirshfeld surface. They enable the identification and quantitative estimation of the relative contributions of different types of intermolecular contacts. Characteristic sharp spikes or distinct regions in the fingerprint plots correspond to specific interactions. Together, these features define the molecular packing and stabilization within the crystal lattice. A portion of the millimetre-sized crystals of $[(C_2H_5)_4N]_3Bi_2I_9$ was crushed into micrometric powder to verify sample purity by X-ray powder diffraction (XRPD). Powder patterns were recorded at room temperature using a PANalytical θ/θ Bragg–Brentano Empyrean diffractometer. The instrument was equipped with CuKα_{1+2} radiations and a PIXcel^{1D} detector. Data were collected over the 5–100° range, with a step size 0.0131°. The total acquisition time was 7 h 30 min.

Differential scanning calorimetry (DSC) measurements were performed on approximately 10 mg of crushed $[(C_2H_5)_4N]_3Bi_2I_9$ crystals. The sample was placed in a closed aluminium crucible. Measurements were carried out in the temperature range 163–373 K at a heating and cooling rate of 10 K min^{-1} using a Sirius NETZSCH DSC 3500 analyzer equipped with a liquid nitrogen cooling system. Thermogravimetric analysis (TGA) and differential thermal analysis (DTA) were performed simultaneously on crushed $[(C_2H_5)_4N]_3Bi_2I_9$ crystals by using a TGA/DTA Q600 SDT (TA Instruments) apparatus. Measurements were carried out in platinum crucibles, with α-Al_2O_3 employed as a reference material. The analyses were conducted under a nitrogen flow of 100 mL min^{-1}. The sample was heated from room temperature to 373 K at a heating rate of 5 K min^{-1}.

Electrical measurements were performed using a Solartron 1260 impedance analyzer controlled by a microcomputer. An AC voltage of 0.5 V was applied over a frequency range from 10^2 Hz to 10^7 Hz. Measurements were performed in the temperature range of 313–368 K. The $[(C_2H_5)_4N]_3Bi_2I_9$ powder was pressed into a dense pellet using a uniaxial hydraulic press. To ensure good electrical contact, both faces of the pellet were coated with a thin layer of silver paste and placed between two polished copper electrodes in a specially designed sample holder.

The temperature was controlled using a programmable furnace and monitored by a thermocouple positioned close to the sample. Complex impedance data (Z' and Z'') were collected and analyzed using ZView software.[32] This analysis allowed modeling of the electrical response and extraction of the bulk resistance, relaxation parameters and electrical conductivity of the material.

3. Results and discussion

3.1. Crystal structure description

The obtained $[(C_2H_5)_4N]_3Bi_2I_9$ crystals are well-defined and exhibit a dark-red prismatic morphology with good

Fig. 1 Typical digital photograph of the $[(C_2H_5)_4N]_3Bi_2I_9$ single crystals.

transparency (Fig. 1). They were grown at room temperature by the slow evaporation of the mother solution, indicating a high degree of crystallinity and phase purity. The crystals show a homogeneous size distribution and the well-developed crystal faces. These features make them suitable for single-crystal X-ray diffraction measurements.

The title compound crystallizes in triclinic system with *P*1 space group at 296 K. The unit cell parameters are as follows: $a = 11.1244\ (4)$ Å, $b = 11.1286\ (4)$ Å, $c = 12.4964\ (5)$ Å, $\alpha = 88.894\ (2)$ °, $\beta = 64.702\ (1)$ °, $\gamma = 61.479\ (1)$ °, $V = 1195.24\ (8)$ Å^3, $Z = 1$. The asymmetric unit consists of three tetraethylammonium $[(C_2H_5)_4N]^+$ cations and one discrete anionic dimer $[Bi_2I_9]^{3-}$. This dimer formed by two BiI_6 octahedra sharing a triangular face (Fig. 2).

This discrete anionic unit is characteristic of $A_3M_2I_9$-type iodometallates ($M = Bi^{3+}$, Sb^{3+}).[33–35] The tetraethylammonium cations play a dual structural role. They ensure overall charge balance by compensating the negative charge of the $[Bi_2I_9]^{3-}$ anions. At the same time, they act as spacers that separate the anionic dimers through weak intermolecular interactions. Halobismuthates(III) display remarkable structural versatility, ranging from zero- to three-dimensional frameworks. This diversity depends on the size, symmetry, and nature of the organic cation, as well as on the halogen involved. Previous studies have shown that most iodobismuthates(III) containing small alkylammonium or unsubstituted heteroaromatic cations adopt the $A_3Bi_2I_9$ stoichiometry.[36–38] This composition generally leads to layered or molecular architectures. The crystal structure of $[(C_2H_5)_4N]_3Bi_2I_9$ can be described as an alternation of inorganic and organic layers along the *b*-axis. The inorganic layers are composed of discrete $[Bi_2I_9]^{3-}$ units, while the organic layers consist exclusively of tetraethylammonium cations (Fig. 3).

The cohesion between the organic and inorganic sublattices is ensured by an extended network of weak C–H···I hydrogen bonds. These interactions are complemented by van der Waals forces (Fig. 4).

The D···A (donor–acceptor) distances range from 4.06(3) to 4.36(2) Å (see Table 4), which is consistent with weak hydrogen bonding. These supramolecular interactions contribute to the three-dimensional stabilization of the crystal lattice. They may also influence the thermal and electrical properties of the compound.

3.2. $[(C_2H_5)_4N]_3Bi_2I_9$ as the only product of slow evaporation

The preparation contained only single crystals of identical colour, with no trace of powder. To check that a few randomly selected crystals had the same crystal structure, they were ground and then analysed by X-ray powder diffraction (XRPD).

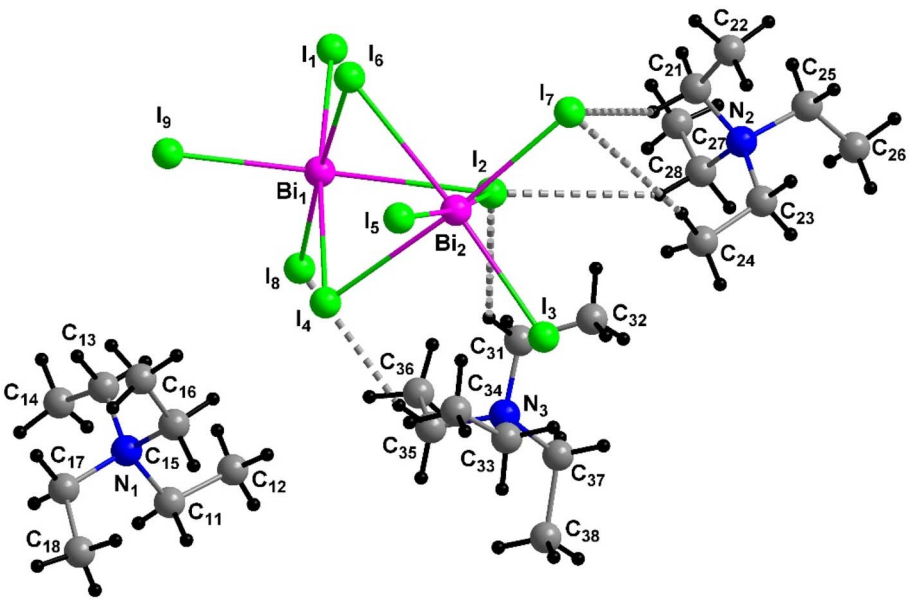

Fig. 2 Asymmetric unit of $[(C_2H_5)_4N]_3Bi_2I_9$. The dashed lines stand for the hydrogen bonds.

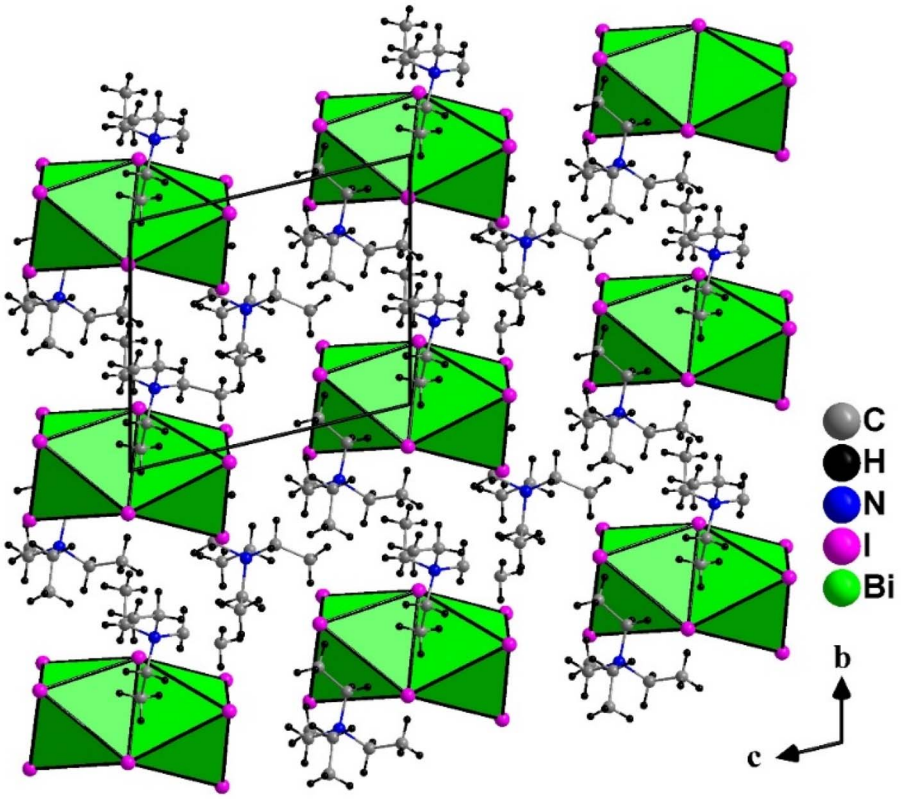

Fig. 3 Projection of the crystal structure of $[(C_2H_5)_4N]_3Bi_2I_9$ in the (*bc*) plane.

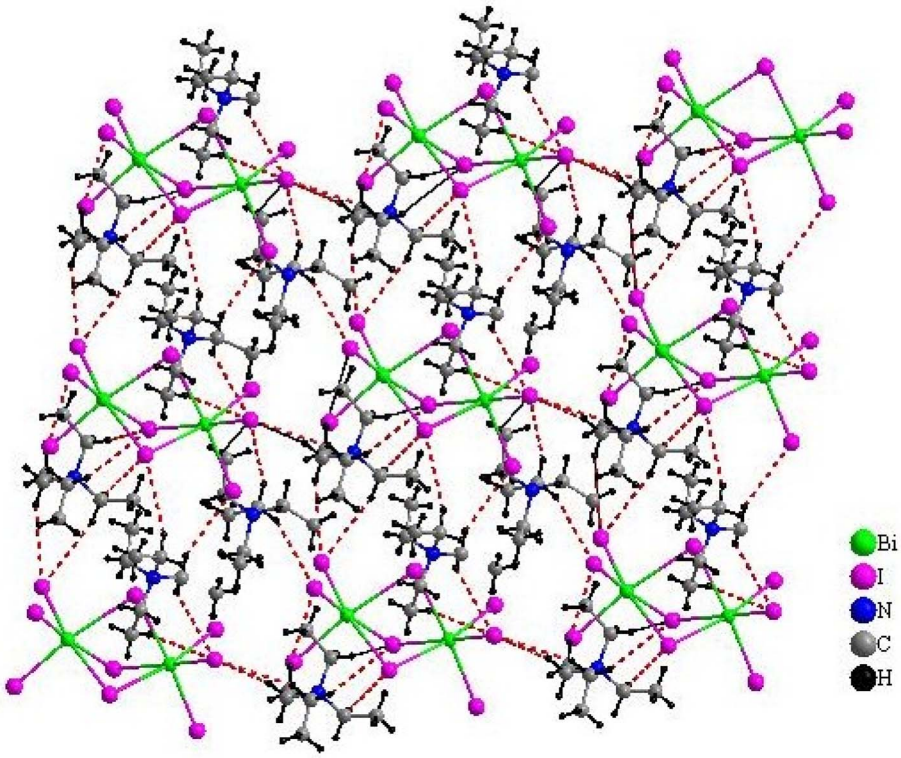

Fig. 4 Hydrogen bonds in the crystal structure of $[(C_2H_5)_4N]_3Bi_2I_9$.

Table 4 Hydrogen-bond geometry (Å, °) for $[(C_2H_5)_4N]_3Bi_2I_9$

D–H···A	D–H (Å)	H···A (Å)	D···A (Å)	D–H···A (°)
C16–H6···I4	0.96	3.30	4.24 (2)	165
C13–H17···I8	0.97	3.48	4.36 (2)	151
C35–H53···I8	0.97	3.24	4.06 (3)	144
C31–H23A···I2	0.97	3.39	4.19 (3)	141
C27–H37···I2	0.97	3.31	4.18 (2)	150
C24–H33···I7	0.96	3.38	4.31 (1)	162
C21–H15···I7	0.97	3.48	4.18 (1)	130

The XRPD pattern of $[(C_2H_5)_4N]_3Bi_2I_9$ was recorded at room temperature, as shown in Fig. 5.

All peaks observed in the XRPD pattern can be indexed with the unit cell parameters and triclinic $P1$ space group determined previously on a single crystal. The triclinic cell parameters determined from the refinement of the XRPD pattern by the Le Bail method[39] of the Fullprof program[40] are $a = 11.1239(5)$ Å, $b = 11.1312(5)$ Å, $c = 12.4921(6)$ Å, $\alpha = 88.894(2)°$, $\beta = 64.710(2)°$ and $\gamma = 61.482(2)°$. These values are very close to those obtained from the single-crystal XRD data of $[(C_2H_5)_4N]_3Bi_2I_9$, confirming the high purity of the preparation.

3.3. Hirshfeld surface analysis

Hirshfeld surface (HS) analysis provides valuable insight into the nature and strength of intermolecular interactions within the crystal structure of $[(C_2H_5)_4N]_3Bi_2I_9$. Fig. 6 displays the Hirshfeld surfaces mapped over three main properties: the normalized contact distance (d_{norm}), the shape index and the curvedness.

The d_{norm} surface highlights regions of close intermolecular contacts through using a color scale. Red areas indicate short contacts with negative d_{norm} values. White regions correspond to distances equal to the sum of the van der Waals radii ($d_{norm} \approx 0$) and blue regions represent longer separations with positive d_{norm} values.[41] The surface is shown as semi-transparent to visualize the atoms of the asymmetric unit, allowing an overall view of the crystal packing. The shape index and curvedness surfaces provide complementary information about the molecular shape and the nature of close contacts. The shape index (middle image in Fig. 5) helps to identify π–π stacking or complementary interactions, which appear as pairs of red and blue triangles on the molecular surface. The curvedness surface (right image in Fig. 5) illustrates the degree of surface curvature. Flat green regions correspond to areas of weak interactions, whereas highly curved blue regions are associated with molecular boundaries.

Fig. 7 presents the 2D fingerprint plots derived from the Hirshfeld surfaces, which quantify the relative contributions of the different intermolecular contacts to the overall crystal packing. For$[(C_2H_5)_4N]_3Bi_2I_9$, the main interactions identified are H···I/I···H, H···H, and I···I.

The H···I/I···H interactions appear as sharp spikes in the fingerprint plots (Fig. 7). These features correspond to contacts where one molecule acts as a hydrogen donor ($d_e > d_i$) and the other as an acceptor ($d_e > d_i$). These contacts dominate the Hirshfeld surface and contribute 58.6% of the total area. The H···H interactions are represented by two broad and symmetrical peaks in the central region of the plot. They account for 40.6% of the total contribution. A minor contribution of 0.8% arises from weak I···I contact. The predominance of H···I/I···H and H···H interactions confirms that hydrogen bonding and van der Waals forces play a major role in stabilizing the crystal structure. Overall, the Hirshfeld surface and fingerprint analyses clearly illustrate the supramolecular architecture and the

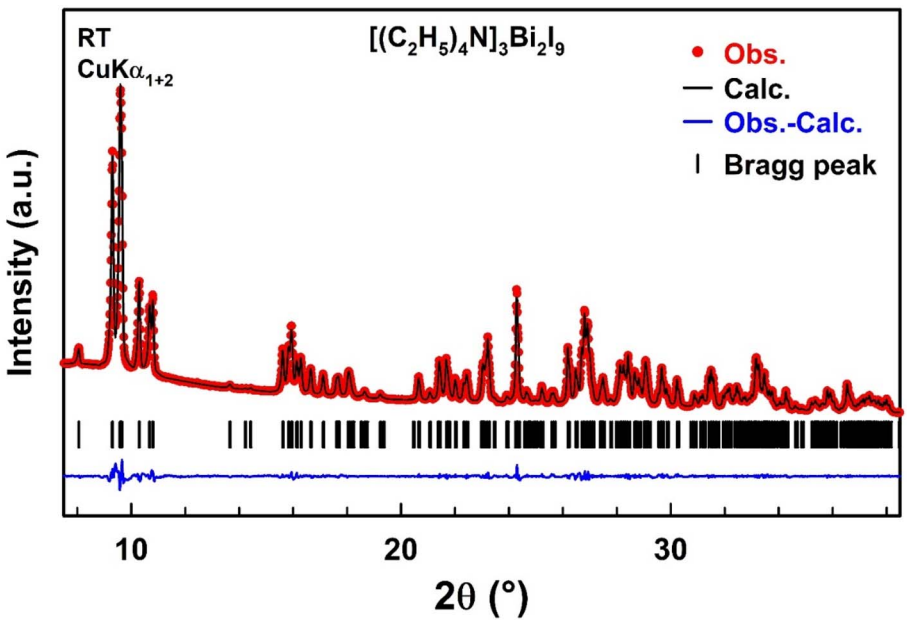

Fig. 5 Comparison of the observed diffraction pattern of $[(C_2H_5)_4N]_3Bi_2I_9$ (red dots) with the pattern calculated by the Le Bail method (black line). The blue curve corresponds to the difference between observed and calculated patterns. Vertical markers give Bragg peak positions (space group $P1$ (no. 1)).

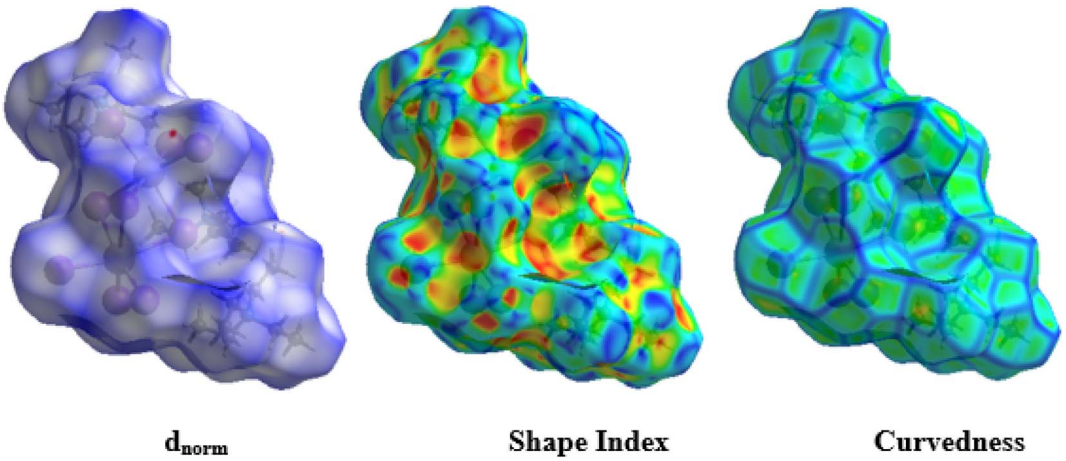

Fig. 6 Hirshfeld surfaces mapped with d_{norm}, shape index and curvedness for $[(C_2H_5)_4N]_3Bi_2I_9$.

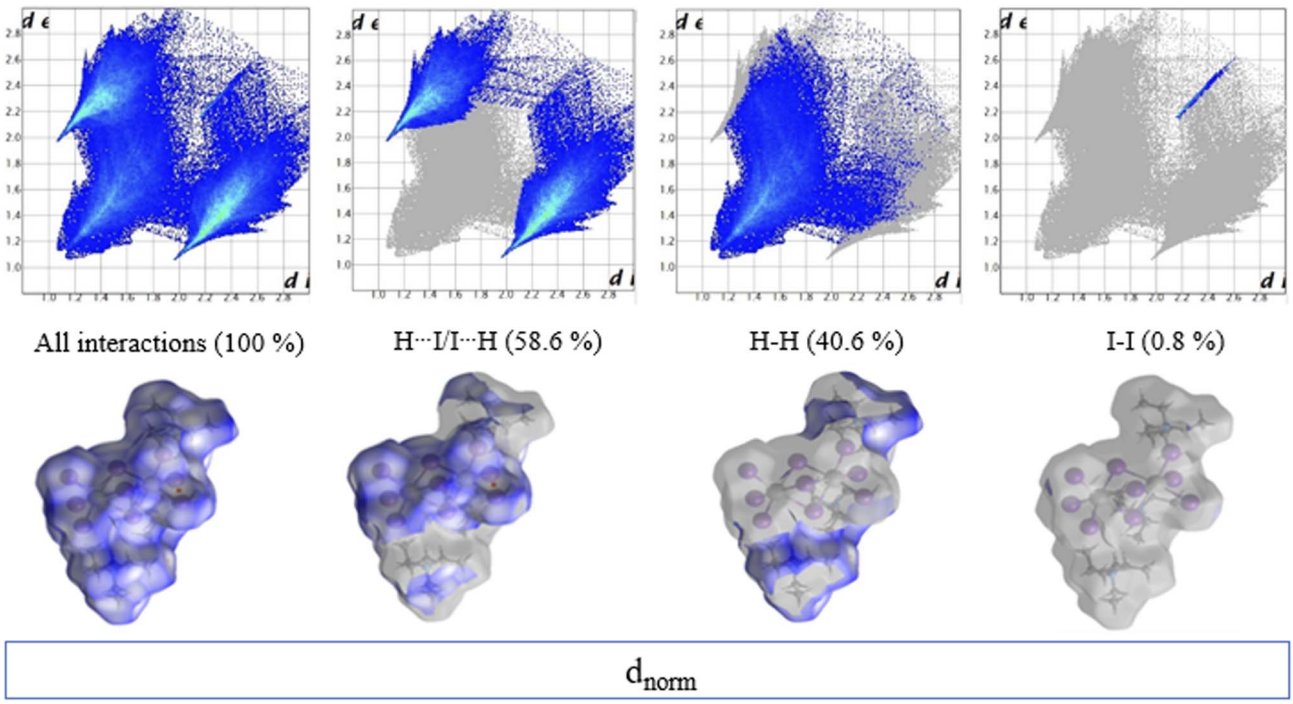

Fig. 7 Two-dimensional fingerprint plot for $[(C_2H_5)_4N]_3Bi_2I_9$ showing contributions from different contacts: I···H/H···I, H–H, I···I.

dominant intermolecular forces governing the packing of $[(C_2H_5)_4N]_3Bi_2I_9$ in the solid state.

3.4. Thermal analysis

The thermal behavior of the $[(C_2H_5)_4N]_3Bi_2I_9$ compound was investigated by Differential Scanning Calorimetry (DSC) and simultaneous Thermogravimetric-Differential Thermal Analyses (TGA-DTA). The DSC thermogram (Fig. 8) recorded under nitrogen atmosphere (10 K min^{-1}) during heating and cooling shows a reversible thermal event. An endothermic peak is observed at 338 K during heating and an exothermic at 331 K upon cooling, confirming the reversibility of this transition.

TGA-DTA analysis was performed under a nitrogen flow at a heating and cooling rate of 5 K min^{-1} over the temperature range from room temperature to 373 K (Fig. 9). No measurable weight loss is observed, indicating that the compound is thermally stable within this interval. The DTA curve exhibits a small endothermic effect at 340 K during heating and a corresponding exothermic effect at 333 K upon cooling. These results are consistent with the DSC measurement. The observed thermal anomaly is attributed to a reversible structural phase transition rather than to decomposition. The reversible thermal event observed between 331 and 340 K is likely related to a structural phase transition. This transition involves an order–disorder process of the organic cations and/or subtle rearrangement of

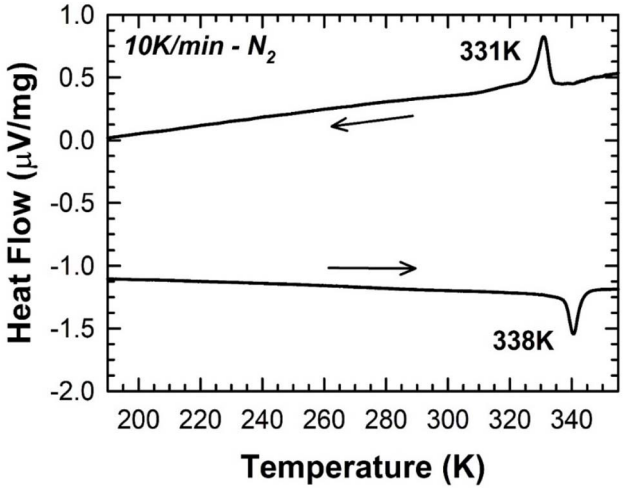

Fig. 8 DSC thermograms collected under N_2 on crushed crystals of $[(C_2H_5)_4N]_3Bi_2I_9$.

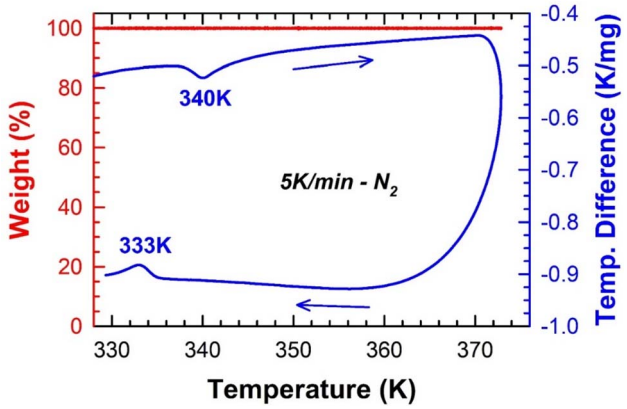

Fig. 9 Thermogravimetric (red) and differential thermal (blue) curves recorded under N_2 during heating and cooling of crushed crystals of $[(C_2H_5)_4N]_3Bi_2I_9$ at a rate of 5 K min^{-1}.

the $[Bi_2I_9]^{3-}$ anionic dimers. In $R_3Bi_2I_9$-type hybrid compounds, such transitions are commonly driven by the dynamic reorientation of the organic cations. This reorientation is often accompanied by modifications of the hydrogen-bonding network. In the present $[(C_2H_5)_4N]_3Bi_2I_9$ compound, the relatively large tetraethylammonium cations may undergo partial ordering upon cooling. This ordering can lead to changes in the C–H···I interactions and slight modifications in the packing of the inorganic framework.

This interpretation is further supported by the electrical measurements. The Arrhenius plot of $\sigma_{DC}T$ reveals two distinct activation energies separated by the transition temperature. This indicates a change in the charge transport barriers associated with the structural reorganization. Moreover, the decrease in the constant phase element (CPE) exponent α with increasing temperature suggests enhanced disorder and a broadening of relaxation times near the transition. Overall, the phase transition appears to involve a combined effect of cation dynamics and minor distortions of the inorganic lattice. This results in a reversible modification of both structural symmetry and electrical response.

Compared with methylammonium-based $R_3Bi_2I_9$ compounds, which typically exhibit phase transitions at slightly lower temperatures and often show less thermal robustness, the present $[(C_2H_5)_4N]_3Bi_2I_9$ compound demonstrates enhanced thermal stability. This improvement can be attributed to the larger tetraethylammonium cation, which influences lattice rigidity and strengthens intermolecular interactions. These effects are consistent with observations reported for bulky organic cations in iodobismuthates.[18–25] These results highlight the important role of cation size in tuning the thermal behavior of zero-dimensional Bi(III) halide hybrids.

3.5. Electrical properties study

3.5.1. Nyquist plots and equivalent circuit. The Nyquist plots ($-Z''$ *vs.* Z') of the $[(C_2H_5)_4N]_3Bi_2I_9$ compound, recorded in the temperature range 313–363 K, are presented in Fig. 10.

Each impedance spectrum exhibits a single depressed semicircular arc. The diameter of this arc decreases progressively with increasing temperature, indicating a thermally activated conduction process.[42,43] The absence of additional semicircles or low-frequency tails suggests that grain boundary and electrode contributions are negligible. Therefore, the overall electrical response is dominated by the bulk (grain) contribution.[44] The observed depression of the semicircles reflects non-Debye relaxation behavior. This behavior is typically associated with a distribution of relaxation times arising from structural or compositional disorder within the material.[45]

To interpret the impedance data, the experimental plots were fitted using an equivalent electrical circuit. The circuit consists of a resistance (R), a capacitance (C), and a constant phase element (CPE) connected in parallel, as shown in the inset of Fig. 10. The good agreement between the experimental data and the fitted curves confirms the adequacy of this model. The electrical parameters extracted from the equivalent circuit fitting are summarized in Table 5.

The CPE is introduced in the equivalent circuit to account for the deviation from ideal Debye behavior. The impedance of a constant phase element is given by:

$$Z_{CPE} = \frac{1}{Q(j\omega)^{\alpha}} \quad (3)$$

where Q is the capacitance of the CPE element, ω is the angular frequency, j is the imaginary unit, and α ($0 \leq \alpha \leq 1$) is the CPE exponent that describes the degree of deviation from ideal capacitance. When $\alpha = 1$, the CPE behaves as a perfect capacitor, while $\alpha = 0$ corresponds to an ideal resistor. Therefore, The parameters Q and α therefore provide valuable insight into the relaxation mechanism and the degree of heterogeneity in the material. As shown in Table 5, the values of α decrease from 0.96 to 0.23 with increasing temperature. This indicates an increasing deviation from ideal Debye behavior and a broadening of the relaxation time distribution. Meanwhile, the increase in Q with temperature reflects enhanced polarization and disorder in the crystal lattice as the system approaches the

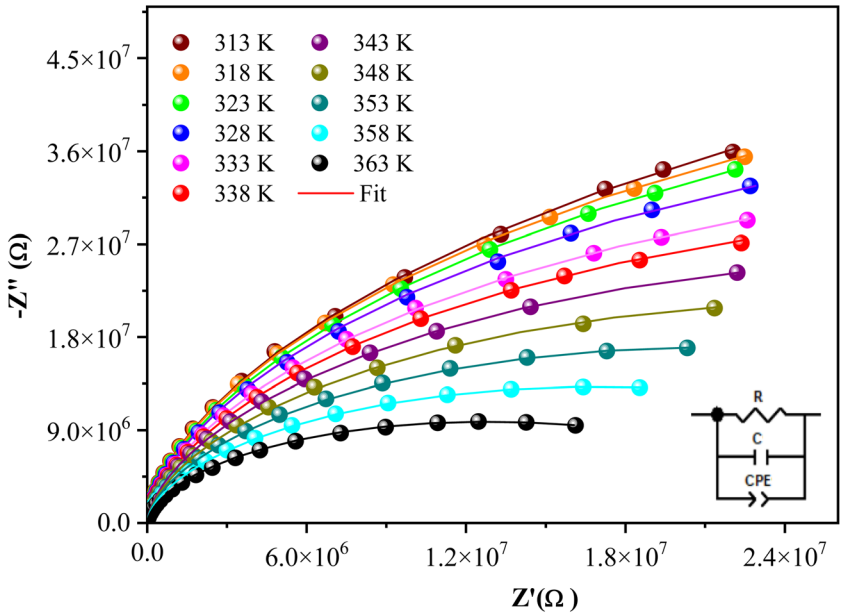

Fig. 10 Temperature dependence of complex impedance (Nyquist plots) at different temperatures.

Table 5 Electrical parameters extracted from the fitted equivalent circuit of $[(C_2H_5)_4N]_3Bi_2I_9$ at different temperatures[a]

Temperature (K)	R (10^8 Ω)	C (10^{-11} F)	Q (10^{-10} F)	α
313	1.690	3.720	4.897	0.9651
318	2.518	5.797	0.622	0.9611
323	5.983	1.092	0.643	0.9588
328	9.348	1.674	0.652	0.9579
333	11.584	3.802	15.09	0.3482
338	13.538	3.828	19.04	0.3276
343	15.755	3.863	34.05	0.2677
348	17.076	3.857	26.42	0.3142
353	19.263	3.934	58.08	0.2307
358	20.578	3.806	38.10	0.2967
363	26.355	3.853	33.69	0.3156

[a] The resistance (R) values increase gradually with temperature, confirming the semiconducting nature of the material and the presence of thermally activated conduction. The capacitance (C) remains almost constant, indicating that the dielectric response mainly arises from bulk polarization effects.

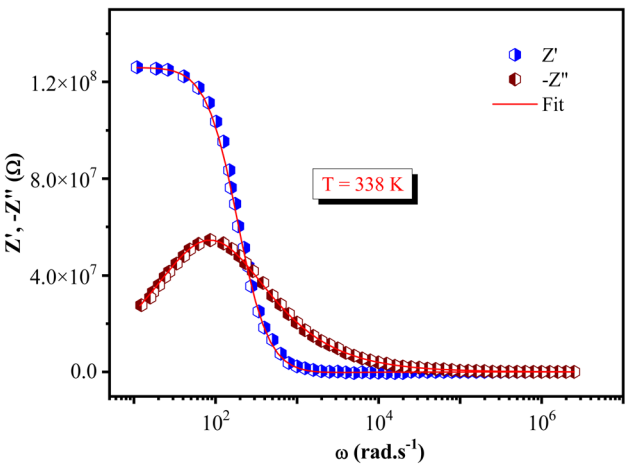

Fig. 11 Frequency dependence of the real (Z') and imaginary (Z'') components of the complex impedance at 338 K.

transition region (around 338 K). At 338 K, the frequency dependence of the real (Z') and imaginary ($-Z''$) components of the impedance (Fig. 11) reveals a single relaxation process. This confirms that the electrical response originates mainly from the bulk contribution. The good agreement between experimental and fitted data demonstrates the validity of the proposed equivalent circuit model.[46–48]

3.5.2. AC conductivity and conduction mechanism. The variation of AC conductivity (σ_{AC}) as a function of angular frequency (ω) at different temperatures for $[(C_2H_5)_4N]_3Bi_2I_9$ is illustrated in Fig. 12.

The conductivity curves reveal that σ_{AC} increases with both frequency and temperature. This behavior is characteristic of materials with a Negative Temperature Coefficient of Resistance (NTCR), typical of semiconductors.[49] At low frequencies, the conductivity remains nearly constant, corresponding to the DC plateau (σ_{DC}). In this region, long-range translational motion of charge carriers dominates. At higher frequencies, σ_{AC} increases in a dispersive region. This reflects localized hopping of charge carriers between energetically favorable sites or defect states within the crystal lattice.[50,51] For the $[(C_2H_5)_4N]_3Bi_2I_9$ compound, the NTCR-type behavior can be attributed to the structural flexibility of the hybrid organic–inorganic framework. It is also related to localized states associated with $[Bi_2I_9]^{3-}$ bi-octahedra and weak C–H···I hydrogen bonds. These features provide suitable pathways for thermally assisted charge carrier hopping. Consequently, the increase in σ_{AC} with temperature demonstrates the thermally activated conduction mechanism,

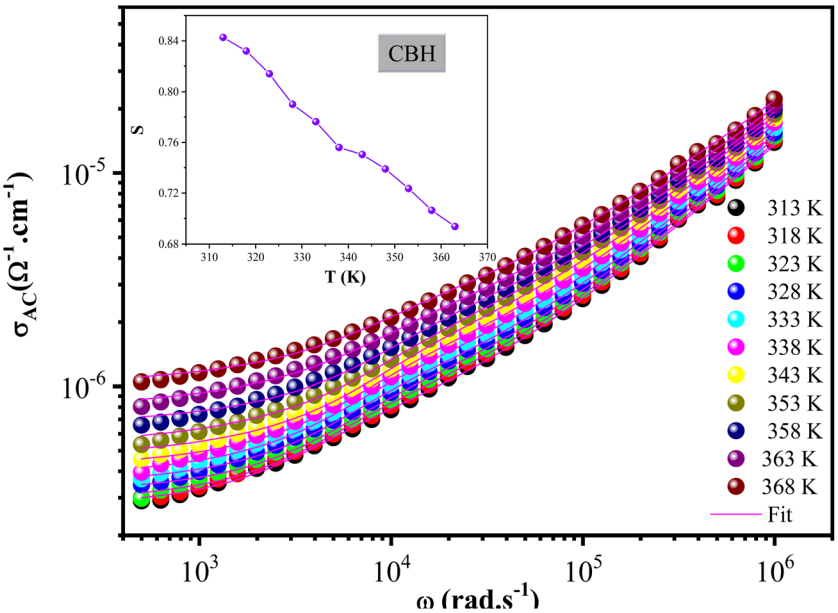

Fig. 12 AC conductivity (σ_{AC}) as a function of angular frequency for the studied material.

consistent with other related $A_3Bi_2I_9$ systems.[52–55] The frequency dependence of σ_{AC} follows Jonscher's universal power law:[56]

$$\sigma_{AC} = \sigma_{DC} + A\omega^{s} \quad (4)$$

where σ_{DC} is the DC conductivity, A is a temperature-dependent pre-exponential factor, and s ($0 < s < 1$) is the frequency exponent. The exponent s reflects the nature of charge carrier interactions with the surrounding lattice. As shown in the inset of Fig. 12, the frequency exponent s gradually decreases with increasing temperature. This trend confirms that the conduction process in $[(C_2H_5)_4N]_3Bi_2I_9$ is well described by the Correlated Barrier Hopping (CBH) model.[57,58] According to this model, charge transport occurs through thermally activated hopping of localized charge carriers. The observed reduction in s with rising temperature indicates a lowering of the effective barrier height. Additional thermal energy enhances the ability of charge carriers to overcome these barriers and move over shorter hopping distances. This behavior further supports the NTCR-type semiconducting character of the compound, where conductivity improves with temperature due to increased charge carrier mobility.

The temperature dependence of the DC conductivity was analyzed using the Arrhenius relation:[59]

$$\sigma_{DC} \times T = \sigma_0 \exp\left(\frac{-E_a}{K_B T}\right) \quad (5)$$

where σ_0 is the pre-exponential factor, E_a is the activation energy, K_B is the Boltzmann constant, and T the absolute temperature.

The Arrhenius plot of $\ln(\sigma_{DC}T)$ *versus* $1000/T$ (Fig. 13) shows two distinct linear regions separated by a transition temperature (T_t) around 338 K. This temperature coincides with the phase transition detected by DSC and DTA analyses.

The extracted activation energies are $E_{a1} = 0.23$ eV in the low-temperature region and $E_{a2} = 0.55$ eV in the high-temperature region. The lower activation energy below T_t suggests enhanced charge carrier mobility in the low-temperature phase. This behavior is likely facilitated by more ordered structural arrangements and stronger intermolecular interactions. Conversely, the higher activation energy above T_t implies an increase in the potential barriers for charge migration. This increase results from the structural reorganization associated with the phase transition. The observed behavior confirms a thermally activated conduction mechanism and the NTCR (Negative Temperature Coefficient of Resistance) characteristic of semiconducting hybrid halides.[60–62]

Similar activation energies and hopping conduction mechanisms have been reported for other Bi(III) hybrid halides. These results confirm that the organic cation strongly affects charge transport through lattice dynamics and disorder.[63–65] This comparison underlines that$[(C_2H_5)_4N]_3Bi_2I_9$ follows the same general trend. However, the larger tetraethylammonium cation modifies the transport behavior near the phase transition. The variation of the natural logarithm of the AC conductivity ($\ln \sigma_{AC}$) as a function of inverse temperature ($1000/T$) at fixed frequencies is depicted in Fig. 14.

The variation of the AC conductivity (σ_{AC}) with temperature was measured at different frequencies. The results reveal two distinct regions. These regions are separated by a transition temperature around 338 K. This value is in perfect agreement with the phase transition detected by DSC analysis.

Activation energies were obtained from the linear fits (Table 6). They show a noticeable decrease with increasing frequency. In the low-temperature phase, E_{a1} decreases from 0.45 eV at 10 Hz to 0.32 eV at 1 kHz. In the high-temperature phase, E_{a2} decreases from 0.15 eV to 0.12 eV over the same frequency range.

This decrease indicates that the applied alternating field facilitates charge carrier motion. It helps them to overcome

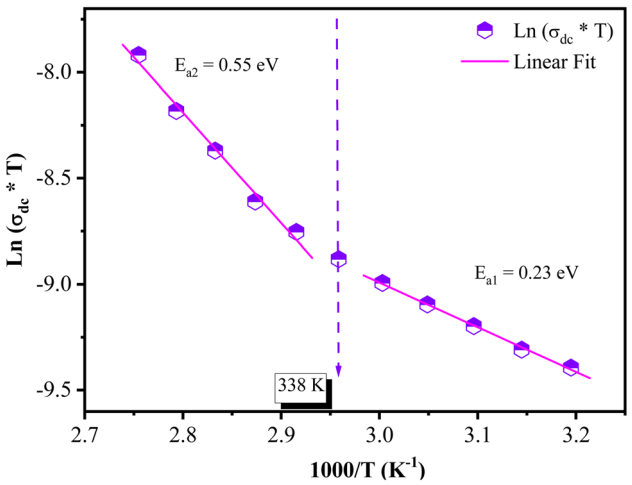

Fig. 13 Temperature dependence of ln($\sigma_{dc} \times T$) as a function of 1000/T.

potential barriers more easily and enhances their hopping between localized states. This trend confirms that the conduction mechanism is thermally activated and mainly governed by hopping, consistent with the Correlated Barrier Hopping (CBH) model. Moreover, when comparing σ_{DC} and σ_{AC} at a given temperature, σ_{AC} values are higher than σ_{DC}. In AC conduction, charge carriers can follow multiple localized hopping paths. In contrast, DC conduction forcescarriers to follow the most energetically favorable long-range paths, which involve larger jumps. This behavior further supports the dominance of the hopping mechanism and indicates a Negative Temperature Coefficient of Resistance (NTCR), which is characteristic of semiconducting materials.[66–68]

These electrical characteristics are particularly attractive for optoelectronic applications. The observed frequency-dependent hopping dynamics and moderate activation energies suggest that $[(C_2H_5)_4N]_3Bi_2I_9$ could be a promising candidate for low-cost hybrid semiconducting devices. Potential applications include photodetectors, light-emitting diodes (LEDs), and photovoltaic absorbers.[69–72]

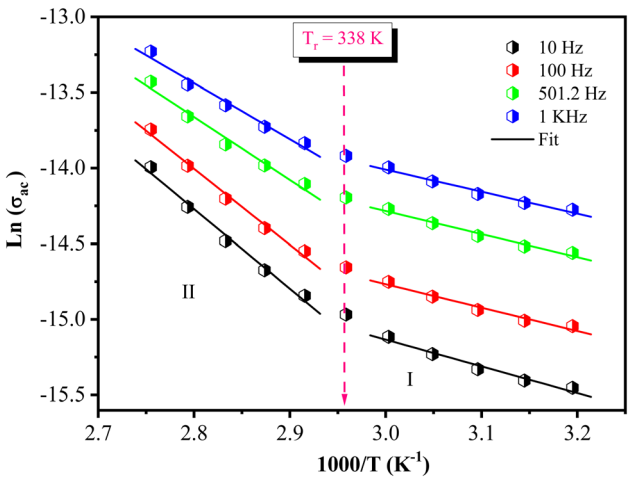

Fig. 14 Arrhenius plots of AC conductivity (ln σ_{AC} *vs.* 1000/T) at various frequencies.

Table 6 Activation energies determined at different frequencies for $[(C_2H_5)_4N]_3Bi_2I_9$

Frequency (Hz)	E_{a1} (eV)	E_{a2} (eV)
10	0.45	0.15
100	0.43	0.13
501.2	0.36	0.13
1000	0.32	0.12

4. Conclusion

In this work, a new lead-free organic–inorganic hybrid compound based on the tetraethylammonium cation, $[(C_2H_5)_4N]_3Bi_2I_9$, has been successfully synthesized and thoroughly characterized. Single-crystal X-ray diffraction analysis revealed that the compound crystallizes in the triclinic system with $P1$ space group. Its zero-dimensional (0D) crystal structure consists of discrete anionic dimers $[Bi_2I_9]^{3-}$ formed by two octahedra sharing a triangular face, and tetraethylammonium $[(C_2H_5)_4N]^+$ cations. The organic and inorganic subunits are interconnected through weak C–H···I hydrogen bonds, which play a crucial role in maintaining the structural integrity and electrostatic equilibrium of the crystal lattice. Hirshfeld surface and fingerprint plot analyses provided quantitative insight into the dominant intermolecular interactions. These analyses highlighting that H···I and H···H contacts play a major role in stabilizing the crystal packing. Thermal analyses (DSC and TGA/DTA) showed a reversible phase transition near 338 K, characterized by an endothermic peak upon heating and an exothermic peak upon cooling. Moreover, the absence of any weight loss up to 373 K confirms the excellent thermal stability of the material within this temperature range. Electrical impedance spectroscopy revealed a Negative Temperature Coefficient of Resistance (NTCR), which is characteristic of semiconducting materials. The frequency-dependent conductivity and activation energy values confirmed that the conduction process is governed by a thermally activated hopping mechanism consistent with the Correlated Barrier Hopping (CBH) model. The combination of structural stability, reversible phase transition, and thermally driven conduction makes $[(C_2H_5)_4N]_3Bi_2I_9$ a promising candidate for optoelectronic and thermally switchable hybrid devices.

Author contributions

Hanen Elgahami: writing – original draft, validation, software, methodology, investigation. Khawla Ben Brahim: writing – original draft, validation, software, methodology, investigation. Sondes Hajlaoui: writing – original draft, visualization, formal analysis. Mona A. Alamri: writing – review & editing, visualization, validation. Gwenaël Corbel: writing – review & editing, visualization, validation. Abderrazek Oueslati: writing – review

& editing, visualization, validation, investigation, formal analysis, data curation.

Conflicts of interest

The authors declare that they have no known competing financial interests or personal relationships that could have appeared to influence the work reported in this paper.

Data availability

The authors confirm that the data used to support the findings of this study are included within the article and are available from the corresponding author upon reasonable request.

CCDC 2457063 contains the supplementary crystallographic data for this paper.[73]

References

1 W.-J. Wei, H.-Q. Gao, Y. Yang, M. Fang, X.-D. Wang, X. Chen, W.-L. Qin, G.-Q. Chen, R.-X. Li, Y.-Z. Tang and Y. Wei, *Chem. Mater.*, 2022, **34**, 6323–6330.
2 J.-M. Gong, T. Shao, P.-Z. Huang, C.-Y. Su, M. Chen, D.-W. Fu and H.-F. Lu, *J. Phys. Chem. C*, 2022, **126**, 15274–15279.
3 Z. Xiao, Z. Song and Y. Yan, *Adv. Mater.*, 2019, **31**, 1803792.
4 R. W. Miles, G. Zoppi and I. Forbes, *Mater. Today*, 2007, **10**, 20.
5 A. K. Jena, A. Kulkarni and T. Miyasaka, *Chem. Rev.*, 2019, **119**, 3036.
6 M. Wang, W. Wang, B. Ma, W. Shen, L. Liu, K. Cao, S. Chen and W. Huang, *Nano-Micro Lett.*, 2021, **13**, 62.
7 S. A. Adonin, I. D. Gorokh, I. D. Gorokh, D. G. Samsonenko, I. V. Yushina, M. N. Sokolov and V. P. Fedin, *CrystEngComm*, 2018, **20**, 7766.
8 S. A. Adonin, M. N. Sokolov, M. E. Rakhmanova, A. I. Smolentsev, I. V. Korolkov, S. G. Kozlova and V. P. Fedin, *Inorg. Chem. Commun.*, 2015, **54**, 89.
9 Y.-H. Liu, H. Peng and W.-Q. Liao, *Chem. Commun.*, 2021, **57**, 647.
10 M. Wojciechowska, A. Gągor, A. Piecha-Bisiorek, R. Jakubas, A. Ciżman, J. K. Zaręba, M. Nyk, P. Zieliński, W. Medycki and A. Bil, *Chem. Mater.*, 2018, **30**, 4597.
11 S. A. Adonin, M. N. Sokolov and V. P. Fedin, *Coord. Chem. Rev.*, 2016, **312**, 1.
12 A. J. Dennington and M. T. Weller, *Dalton Trans.*, 2018, **47**, 3469.
13 J. Zaleski, C. Pawlaczyk, R. Jakubas and H. G. Unruh, *J. Condens. Matter Phys.*, 2000, **12**, 7509.
14 S. A. Adonin, D. G. Samsonenko, M. N. Sokolov and V. P. Fedin, *Russ. J. Coord. Chem.*, 2016, **42**, 27.
15 F. Zhang, H. Lu, J. Tong, J. J. Berry, M. C. Beard and K. Zhu, *Energy Environ. Sci.*, 2020, **13**, 1154.
16 W. Li, A. Stroppa, Z.-M. Wang and S. Gao, *Hybrid Organic Inorganic Perovskites*, Wiley-VCH, 2020.
17 W. Li, Z. Wang, F. Deschler, S. Gao, R. H. Friend and A. K. Cheetham, *Nat. Rev. Mater.*, 2017, **2**, 16099.
18 S. Yakunin, Y. Shynkarenko and M. V. Kovalenko, *Inorg. Chem.*, 2018, **57**, 15332–15340.
19 A. Jain, A. Voznyy and O. M. Bakr, *J. Mater. Chem. A*, 2019, **7**, 16832–16841.
20 M. Roknuzzaman and K. Ostrikov, *Phys. Chem. Chem. Phys.*, 2020, **22**, 21906–21915.
21 J. Li, Z. Zhang and H. Fu, *J. Phys. Chem. C*, 2017, **121**, 24646–24653.
22 E. Greul and S. D. Stranks, *Adv. Funct. Mater.*, 2018, **28**, 1704443.
23 K. Brandt and M. C. Weidman, *Chem. Mater.*, 2019, **31**, 2728–2736.
24 P. Maheshwari and R. Singh, *Dalton Trans.*, 2020, **49**, 11234–11242.
25 L. Z. Tan and A. M. Rappe, *J. Mater. Chem. C*, 2021, **9**, 2341–2350.
26 M. Yuan, L. N. Quan, R. Comin, G. Walters, R. Sabatini, O. Voznyy, S. Hoogland, Y. Zhao, E. M. Beauregard, P. Kanjanaboos, Z. Lu, D. H. Kim and E. H. Sargent, *Nat. Nanotechnol.*, 2016, **11**, 872.
27 G. M. Sheldrick, *SADABS, Program for Empirical Absorption Correction of AreaDetector Data*, University of Gottingen, Germany, 1996, p. , p. 467.
28 G. M. Sheldrick, *SHELXL-97*, Program of Crystal Structure Refinement University of Gottingen, 1997, vol. 112.
29 L. J. Farrugia, WinGX suite for small-molecule single-crystal crystallography, *Appl. Crystallogr.*, 1999, **32**, 837.
30 M. Riedel, J. Ristein and L. Ley, The impact of ozone on the surface conductivity of single crystal diamond, *Diamond Relat. Mater.*, 2004, **13**, 746–750.
31 S. K. Wolff, D. J. Grimwood and J. J. McKinnon, *et al.*, *Crystal Explorer 3.0*, University of Westren Australia, Perth, 2007, 2005–2013.
32 *ZView Software User's Guide*, Scribner Associates Inc., version 3.5, 2012.
33 M. Abulikemu, S. Ould-Chikh, X. Miao, E. Alarousu, B. Murali, G. O. Ngongang Ndjawa, J. Barbé, A. El Labban, A. Amassian and S. Del Gobbo, *J. Mater. Chem. A*, 2016, **4**, 12504–12515.
34 R. L. Z. Hoye, R. E. Brandt, A. Osherov, V. Stevanović, S. D. Stranks, M. W. B. Wilson, H. Kim, A. J. Akey, J. D. Perkins, R. C. Kurchin, J. R. Poindexter, E. N. Wang, M. G. Bawendi, V. Bulović and T. Buonassisi, *Chem.–Eur. J.*, 2016, **22**, 2605–2610.
35 J. Möbs, S. Pan, R. Tonner-Zech and J. Heine, *Dalton Trans.*, 2022, **51**, 13771–13778.
36 S. Sun, S. Tominaka, J.-H. Lee, F. Xie, P. D. Bristowe and A. K. Cheetham, *arXiv*, 2015, preprint, arXiv:1509.08126, DOI: 10.48550/arXiv.1509.08126.
37 S. Oez, J. Hebig, E. Jung, T. Singh, A. Lepcha, S. Olthof, J. Flohre, Y. Gao, R. German, P. H. M. Van Loosdrecht, K. Meerholz, T. Kirchartz and S. Mathur, *Sol. Energy Mater. Sol. Cells*, 2016, **144**, 324.
38 P. Szklarz, A. Pietraszko, R. Jakubas, G. Bator, P. Zieliński and M. Gałązka, *J. Phys.:Condens. Matter*, 2008, **20**, 255221.
39 A. A. Le Bail, H. H. Duroy and J. L. J. L. Fourquet, *Mater. Res. Bull*, 1988, **23**, 447–452.

40 J. Rodriguez Carvajal, *Phys. B*, 1993, **192**, 55–69.
41 P. Szklarz, M. Owczarek, G. Bator, *et al.*, *J. Mol. Struct.*, 2009, **929**, 48–57.
42 H. Elgahami, M. Ajili, T. Roisnel and A. Oueslati, *J. Solid State Chem.*, 2022, **311**, 123108.
43 M. Ben Gzaiel, A. Oueslati, F. Hlel and M. Gargouri, *Phys. E*, 2016, **83**, 405.
44 H. Elgahami, J. Lhoste, S. Auguste, G. Corbel and A. Oueslati, *J. Solid State Chem.*, 2022, **314**, 123357.
45 M. Kar and T. Körzdörfer, *Mater. Res. Express*, 2020, **7**, 055502.
46 F. A. Gulotta, M. A. Montenegro, L. Vergara Diaz, *et al.*, *Microchem. J.*, 2023, **190**, 108689.
47 A. Moulahi, O. Guesmi, M. S. M. Abdelbaky, *et al.*, *J. Alloys Compd.*, 2022, **898**, 162956.
48 M. Horchani, A. Omri, A. Benali, *et al.*, *J. Solid State Chem.*, 2022, **308**, 122898.
49 A. Jonscher, *Nature*, 1977, **267**, 673–679.
50 M. M. El-Nahass, *et al.*, *Solid State Ionics*, 2005, **176**, 1583–1592.
51 M. S. Hussain, *et al.*, *J. Mater. Chem. C*, 2021, **9**, 14603–14614.
52 M. A. Subramanian, *et al.*, *Adv. Mater.*, 2013, **25**, 1–25.
53 M. R. Filip and F. Giustino, *J. Phys. Chem. C*, 2016, **120**, 166–173.
54 S. P. Singh, *et al.*, *J. Alloys Compd.*, 2020, **844**, 156160.
55 M. Z. Ahmad, *et al.*, *J. Solid State Chem.*, 2022, **312**, 123146.
56 Z. Siddique, *et al.*, *J. Mater. Chem. C*, 2023, **11**, 223–234.
57 S. R. Elliott, *Philos. Mag. B*, 1977, **36**, 1291–1304.
58 S. R. Elliott, *Adv. Phys.*, 1987, **36**, 135–217.
59 X. Li, *et al.*, *Materials*, 2023, **16**, 4490.
60 Z. Wu, *et al.*, *Nanoscale*, 2023, **15**, 5598–5622.
61 H. Ben Attia, F. Bentahar, M. S. M. Abdelbaky, *et al.*, *J. Alloys Compd.*, 2023, **969**, 172317.
62 P. Yadav and A. Sharma, *AIP Conf. Proc.*, 2016, **1728**, 020189.
63 S. Zaghden, H. Ben Attia, M. S. M. Abdelbaky, *et al.*, *ACS Omega*, 2024, **9**, 47597–47612.
64 I. B. H. Sadok, F. Hajlaoui, K. Karoui, N. Audebrand, Th. Roisnel and N. Zouari, *J. Phys. Chem. Solids*, 2019, **129**, 71.
65 S. P. Singh, *et al.*, *J. Alloys Compd.*, 2020, **844**, 156160.
66 M. Z. Ahmad, *et al.*, *J. Solid State Chem.*, 2022, **312**, 123146.
67 Z. Jin, *et al.*, *J. Mater. Chem. A*, 2020, **8**, 16166–16188.
68 Z. Siddique, *et al.*, *J. Mater. Chem. C*, 2023, **11**, 223–234.
69 X. Li, *et al.*, *Materials*, 2023, **16**, 4490.
70 Z. Wu, *et al.*, *Nanoscale*, 2023, **15**, 5598–5622.
71 S. Brahma, R. N. P. Choudhary and S. A. Shivashankar, *J. Phys. Chem. Solids*, 2012, **73**, 357–362.
72 M. Okutan, E. Basaran, H. I. Bakan and F. Yakuphanoglu, *J. Phys. B*, 2005, **364**, 300–305.
73 CCDC 2457063: Experimental Crystal Structure Determination, 2025, DOI: 10.5517/ccdc.csd.cc2ngs31.